Supplementary Information (SI) for Journal of Materials Chemistry C.

Shaping scintillation and UV-VIS-NIR luminescence properties through synergistic lattice disordered engineering and exciton-mediated energy transfer in Pr^{3+}-doped $Lu_{1.5}Y_{1.5}Al_{5-x}Sc_xO_{12}$ (x = 0.0 - 2.0) garnets

Karol Bartosiewicz[1]*, Yevheniia Smortsova[2], Piotr Radmoski[3], Marcin E. Witkowski[4], Konrad J. Drozdowski[4], Masao Yoshino[5,6], Takahiko Horiai[5,6], Damian Szymański[7], Wioletta Dewo[3], Justyna Zeler[8], Paweł Socha[9], Maksym Buryi[10], Andrey Prokhorov[1,10], David John[1,11,12], Jakub Volf[1,13], Tomasz Runka[3], Tomasz Pędziński[14], Karol Hauza[14], Vítězslav Jarý[1], Yasuhiro Shoji[5,6], Kei Kamada[5,6], Eugeniusz Zych[8], Winicjusz Drozdowski[3], Akira Yoshikawa[5,6]

[1] Institute of Physics, Academy of Sciences of the Czech Republic, Na Slovance 1999/2, 18200, Prague, Czechia
[2] Deutsches Elektronen-Synchrotron DESY, Notkestr. 85, Hamburg 22607, Germany
[3] Faculty of Materials Engineering and Technical Physics, Poznan University of Technology, Piotrowo 3, 60-965, Poznań, Poland;
[4] Institute of Physics, Faculty of Physics, Astronomy and Informatics, Nicolaus Copernicus University in Toruń, ul. Grudziądzka 5, 87100, Toruń, Poland
[5] Institute for Materials Research, Tohoku University, 2-1-1 Katahira Aoba-ku, Sendai, Miyagi 9808577, Japan
[6] New Industry Creation Hatchery Center, Tohoku University, Sendai, Miyagi, Japan
[7] Institute of Low Temperature and Structure Research, Polish Academy of Sciences, Wrocław, Poland
[8] Faculty of Chemistry, University of Wrocław, Joliot-Curie Street 14 F, 50383, Wrocław, Poland
[9] Łukasiewicz Research Network - Institute of Microelectronics and Photonics, Aleja Lotników 32/46, 02-668, Warsaw, Poland
[10] Institute of Plasma Physics of the Czech Academy of Sciences, U Slovanky, 2525/1a, Prague, 182 00, Czech Republic
[11] Faculty of Nuclear Sciences and Physical Engineering, Czech Technical University, Břehová 7, 115019, Prague, Czech Republic,
[12] Nuclear Physics Institute of the Czech Academy of Sciences, Na Truhlářce 39/64, 18000, Prague, Czech Republic,
[13] Department of Inorganic Chemistry, University of Chemistry and Technology, Technická 5, 166 28, Prague, Czech Republic
[14] Faculty of Chemistry, Adam Mickiewicz University in Poznań, Uniwersytetu Poznańskiego 8, 61-614 Poznan, Poland

***Corresponding author email:** *Karol Bartosiewicz (bartosiewicz@fzu.cz)*

SUPPLEMENTARY INFORMATION

1. NIR-VIS-UV absorption spectra

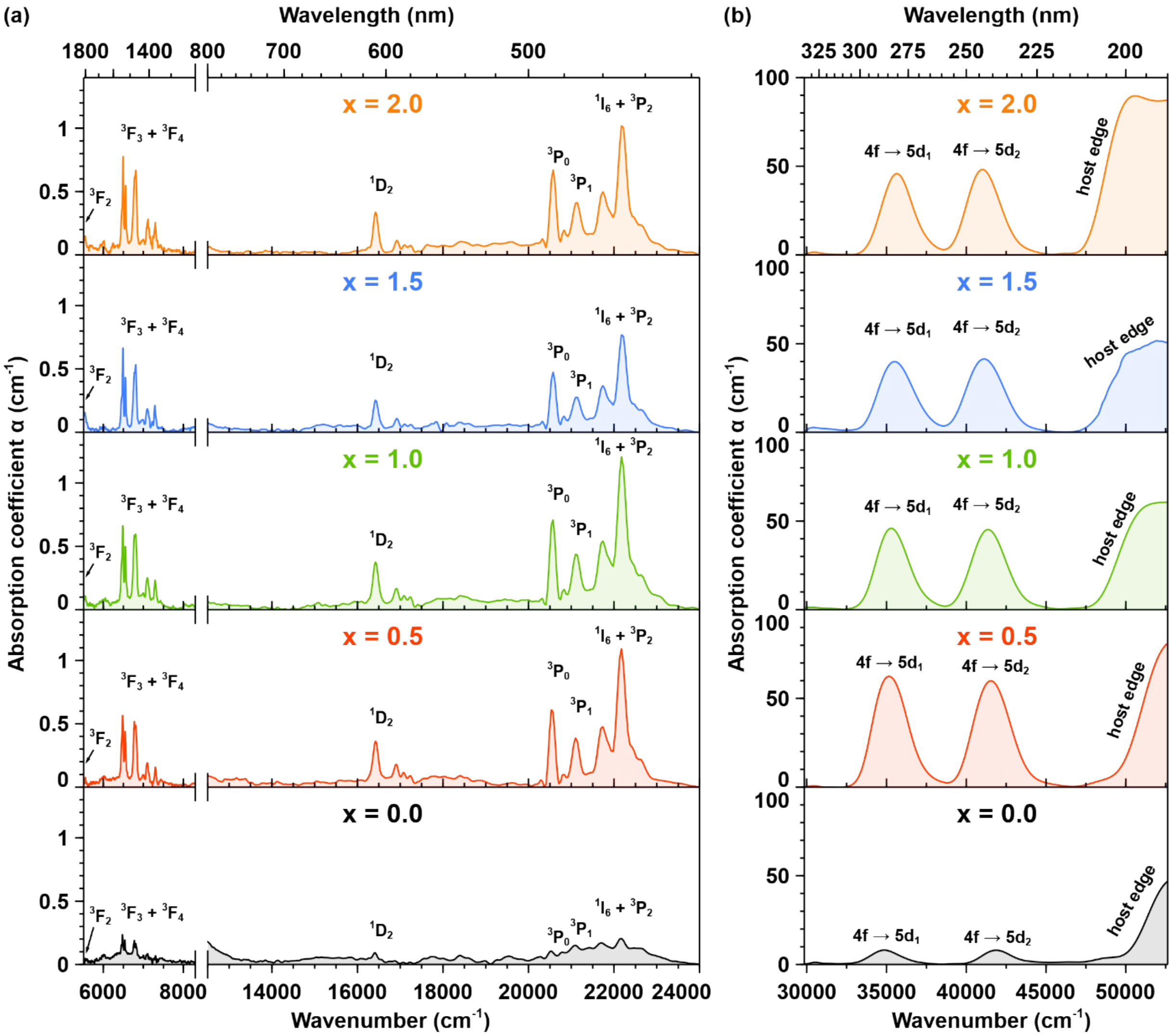

Figure S1. Room-temperature unpolarized optical absorption spectra of the Pr^{3+}-doped $Lu_{1.5}Y_{1.5}Al_{5-x}S_xO_{12}$ crystals with increasing Sc^{3+} ions concentration recorded in (a) near-infrared (NIR, 1800 - 1300 nm) and visible (VIS, 400 - 670 nm) and (b) ultraviolet (UV, 190 - 330 nm) spectral regions.

The absorption spectra complement the excitation and emission spectra (see Figure 5a and 5b), demonstrating that with increasing Sc^{3+} ions concentration, both the interconfigurational $4f^2 \rightarrow 5d_{1,2}^{1}4f^{1}$ absorption bands and intraconfigurational $4f^2 \rightarrow 4f^2$ absorption lines of Pr^{3+} ions exhibit enhanced intensity within the NIR-VIS-UV spectral regions. This enhancement is attributed to the improved radial distribution of Pr^{3+} ions and the reduced local symmetry around them, resulting from increased lattice disorder introduced by Sc substitution. These findings show that Sc admixing efficiencly modifies the local environment of Pr^{3+} ions, leading to strengthened optical absorption, which is significant for enhancing the performance of Pr^{3+}-doped optical materials.

2. *Raman spectroscopy*

Table S1. The experimental wavenumbers (cm^{-1}) and assignment of Raman modes for the Pr^{3+}-doped $Y_{1.5}Lu_{1.5}Al_{5-x}Sc_xO_{12}$ crystals, where x = 0.0, 0.5, 1.0, 1.5 and 2.0, alongside auxiliary values for $Y_3Al_5O_{12}$ crystal measured by Poulos *et al.* [1].

$Y_{1.5}Lu_{1.5}Al_{5-x}Sc_xO_{12}$					$Y_3Al_5O_{12}$ [1]	Symmetry Type	Assignment [2-4]
x = 0.0	x = 0.5	x = 1.0	x = 1.5	x = 2.0			
cm^{-1}	cm^{-1}	cm^{-1}	cm^{-1}	cm^{-1}	cm^{-1}		
155	144	141	142	143	145	F_{2g}	Lu^{3+}/Y^{3+}/Pr^{3+} Translations
135	131	130	129	128	163	E_g	
-	-	-	-	-	220	F_{2g}	
240	237	236	231	225	243	F_{2g}	Translations + + Librations + + ν_3 ($Al_{5-x}Sc_xO_4$)
260	257	256	253	250	261	F_{2g}	
-	-	-	-	-	295	F_{2g}	
336	334	333	325	319	310	E_g	

-	-	-	-	-	340	E_g	
-	-	-	-	-	361	F_{2g}	
374	378	379	379	381	370	A_{1g}	
-	-	-	-	-	372	F_{2g}	
398	392	389	384	374	402	E_g	
410	412	414	416	399	406	F_{2g}	
-	-	-	-	-	438	F_{2g}	
-	-	-	-	-	523	E_g	
537	535	534	534	537	536	E_g	
548	549	546	545	547	545	F_{2g}	ν_2 ($Al_{5-x}Sc_xO_4$)
563	-	-	-	-	559	A_{1g}	
699	694	691	687	681	691	F_{2g}	$\nu_1 + \nu_4$ ($Al_{5-x}Sc_xO_4$)
-	-	-	-	-	712	E_g	
725	720	717	718	722	718	F_{2g}	
763	761	-	-	-	754	E_g	
790	785	783	778	767	783	A_{1g}	
864	857	854	847	837	857	F_{2g}	
-	-	-	-	-	-	F_{2g}	

3. *Thermal modification of Pr^{3+} photoluminescence characteristics*

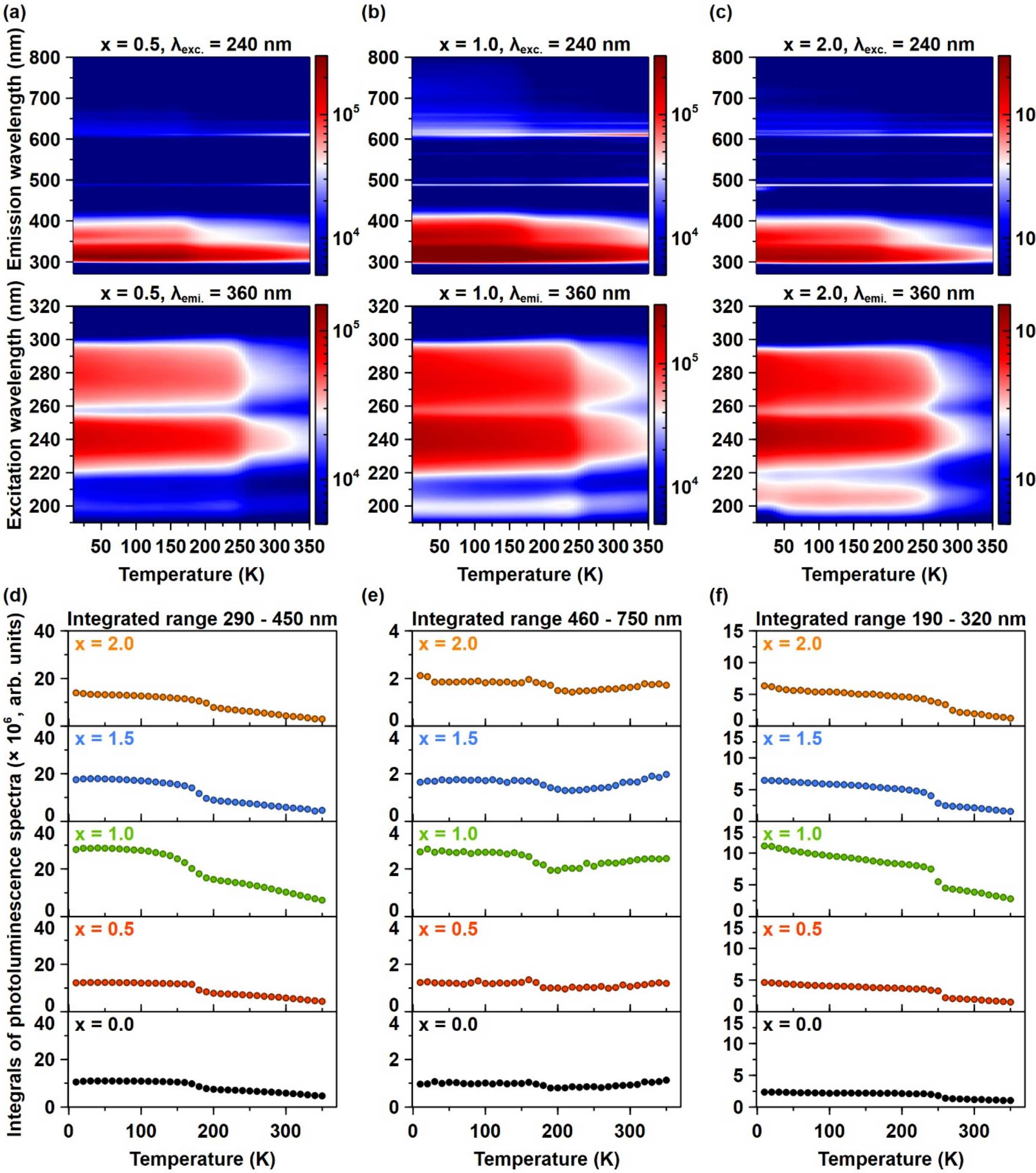

Figure S2. 2D temperature-dependent (10 - 350 K) maps of photoluminescence emission (upper panels, λ_{exc} = 240 nm) and excitation spectra (lower panels, λ_{emi} = 360 nm) for the Pr^{3+}-doped

$Y_{1.5}Lu_{1.5}Al_{5-x}Sc_xO_{12}$ crystals, where (a) x = 0.5, (b) x = 1.0, and (c) x = 2.0. Temperature dependence of (d) integrated photoluminescence intensity in the 290 - 450 nm spectral range, (e) integrated PL intensity in the 460 - 750 nm spectral range, (f) integrated photoluminescence excitation intensity in the 190 - 320 nm spectral range for the $Lu_{1.5}Y_{1.5}Al_{5-x}Sc_xO_{12}$ crystals with increasing Sc^{3+} ions concentrations.

The photoluminescence characteristics of Pr^{3+} ions in the $Lu_{1.5}Y_{1.5}Al_{5-x}Sc_xO_{12}$ crystals demonstrate pronounced temperature and Sc concentration-dependent behaviors. Integrated photoluminescence emission within the 290 - 450 nm spectral range (refer to Figure S2d), associated with the the interconfigurational $4f^15d_1^1 \rightarrow 4f^2$ electronic transition, exhibits a systematic decline with increasing temperature, attributable to thermal quenching mechanisms. Notably, higher scandium concentrations ($x \geq 1.5$) manifest more substantial intensity attenuation. The Pr^{3+}-doped $Y_{1.5}Lu_{1.5}Al_{5-x}Sc_xO_{12}$ crystals with scandium concentrations exceeding $x \geq 1.0$ reveal significantly enhanced integrated luminescence intensities across the 10 - 300 K temperature range, suggesting complex luminescence enhancement phenomena. Conversely, the integrated PL emission in the 460 – 750 nm spectral range (refer to Figure S2e), corresponding to the intraconfigurational $4f^2 \rightarrow 4f^2$ transitions, demonstrates a non-linear temperature dependence. The observed irregular trend - characterized by initial intensity decrease up to approximately 180 K, followed by subsequent intensity augmentation - can be attributed to thermally activated *4f* energy state population and increased lattice disorder, particularly pronounced in high scandium concentration samples. Photoluminescence excitation intensity within the 190 - 320 nm spectral region (refer to Figure S2f), demonstrates a consistent decline with temperature elevation. This decline becomes more pronounced with increasing scandium concentrations, indicating that structural modifications induced by scandium admixing significantly impact excitation efficiency. Interestingly, scandium-admixed crystals exhibit substantially enhanced photoluminescence and excitation intensities compared to the Pr^{3+}-doped $Lu_{1.5}Y_{1.5}A_5O_{12}$ (x = 0.0) crystal. The optimal luminescence performance is achieved with moderate scandium concentration (x = 1.0), which effectively balances thermal stability and emission intensity. At higher scandium concentrations, lattice distortions simultaneously enhance non-radiative decay pathways and enable thermally activated luminescence mechanisms.

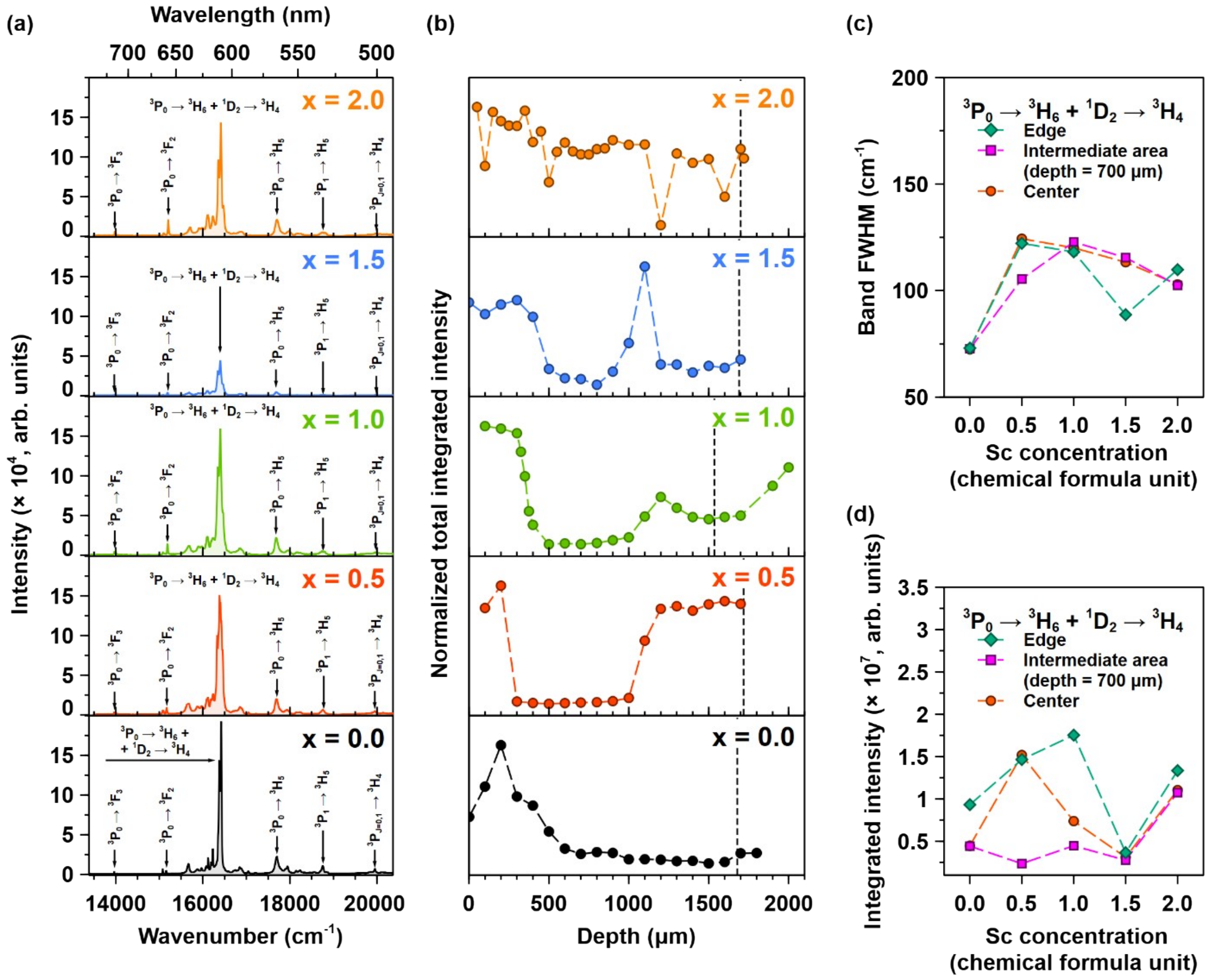

Figure S3. (a) Room temperature high spatial resolution emission spectra of the Pr^{3+}-doped $Lu_{1.5}Y_{1.5}Al_{5-x}Sc_xO_{12}$ crystals with increasing Sc^{3+} ions concentration exited at 488 nm. (b) The radial variation in emission intensity corresponding to the $^3P_0 \rightarrow {}^3H_6$ and $^1D_2 \rightarrow {}^3H_4$ transitions of Pr^{3+} ions as a function of increasing Sc^{3+} ion concentration. (c) The full width at half maximum (FWHM) of the $^3P_0 \rightarrow {}^3H_6 + {}^1D_2 \rightarrow {}^3H_4$ multiple emission lines. (d) Integrated emission lines recorded in the 605 - 615 nm spectral range assigned to the $^3P_0 \rightarrow {}^3H_6 + {}^1D_2 \rightarrow {}^3H_4$ transitions of Pr^{3+} ions.

Figure S3a presents high-resolution spatial emission spectra of Pr^{3+}-doped $Lu_{1.5}Y_{1.5}Al_{5-x}Sc_xO_{12}$ crystals under 488 nm excitation. Notably, the samples containing Sc exhibit slightly enhanced

Pr^{3+} emission intensity compared to their Sc-free counterpart. The emission spectra further reveal broadened and overlapping spectral lines, which provide further evidence of increased structural disorder within the host lattice.

To determine the radial distribution of Pr^{3+} ions in the $Lu_{1.5}Y_{1.5}Al_{5-x}Sc_xO_{12}$ crystals with varying Sc^{3+} ion concentrations, the luminescence intensities corresponding to the $^3P_0 \rightarrow {}^3H_6 + {}^1D_2 \rightarrow {}^3H_4$ transitions of Pr^{3+} ions were measured across the crystal from the rim to the core (refer to Figure S3b). The integrated emission intensity within these spectral regions reflects a dependence on both the concentration of Pr^{3+} ions and the degree of structural disorder in the host lattice. These findings provide crucial insights into the interplay between dopant distribution and host lattice characteristics, enabling a more comprehensive understanding of the segregation mechanism. All examined crystals exhibit a pronounced enrichment of Pr^{3+} ions at the edges, with a progressive decrease in concentration toward the crystal center. This behavior likely arises due to a weak lattice modification and lower facilitation of dopant diffusion. However, as the Sc^{3+} ion concentration increases, the steep gradient in Pr^{3+} distribution shifts significantly toward the central region, resulting in improved homogeneity in Pr^{3+} ion distribution. The steep decrease in Pr^{3+} luminescence intensity towards the crystal core illustrates that the Pr^{3+} ions are preferentially localized around the rim and exhibit limited diffusion toward the center. This effect reflects enhanced dopant diffusion throughout the crystal, likely due to increased lattice disorder induced by the substitution of Sc^{3+} ions. The lattice disorder diminishes the energy barriers for the migration of Pr^{3+}, allowing deeper penetration into the crystal. Consequently, the Pr^{3+} ions achieve a more even distribution in the radial profile. Notably, an increase in Pr^{3+} concentration is observed in the intermediate region (~1200 μm depth) in Sc-admixed crystals. This intermediate region correlates closely with the presence of point-like features, manifesting as rounded spots embedded within the main crystal structure (see Figure 2 and 3). These findings strongly support the conclusion that crystallization within the crucible occurs locally and independently within each of the five crystallization capillaries, thereby disrupting global uniform crystallization. This localized crystallization mechanism underscores the impact of Sc^{3+} doping on spatial dopant distribution and crystal growth dynamics. A distinct behavior and distribution pattern of Pr^{3+} ions is observed in the Pr^{3+}-doped $Y_{1.5}Lu_{1.5}Al_3Sc_2O_{12}$ ($x = 2.0$) crystal, which exhibit an hypoeutectic structure. This hypoeutectic arrangement significantly alters the segregation mechanism of Pr^{3+} ions, as they become incorporated into both the garnet and perovskite phases. Consequently, the formation of hypoeutectic structures emerges as a promising strategy for mitigating radial segregation of highly mismatched elements. This approach offers valuable potential for enhancing the uniformity of dopant distribution in complex crystalline materials.

Figure S3c compares the FWHM of the dominant $^3P_0 \rightarrow {}^3H_6 + {}^1D_2 \rightarrow {}^3H_4$ emission lines in the edge, intermediate, and core regions for all examined crystals. Samples containing Sc^{3+} ions exhibit significantly broadened emission lines, with similar broadening observed across all three regions. This finding provides further evidence of increased host lattice disorder induced by Sc^{3+} incorporation. An exception is noted in the hypoeutectic crystal, which demonstrates comparable FWHM across all regions due to the presence of two distinct, non-mixed phases. Figure S3d compares the integrated emission intensity of $^3P_0 \rightarrow {}^3H_6 + {}^1D_2 \rightarrow {}^3H_4$ transitions in the edge, intermediate, and core regions for all crystals. The integrated emission intensity reveals irregular trends across these regions and varying Sc^{3+} ions concentrations. This observation aligns with the SEM-EDS results (Figure 2 and 3), reinforcing the conclusion that crystallization within the crucible occurs locally and independently within each of the five crystallization capillaries, thereby disrupting global uniform crystallization. The hypoeutectic crystal, again, serves as an exception, showing consistent emission intensities across all regions, attributable to the coexistence of two distinct, non-mixed phases.

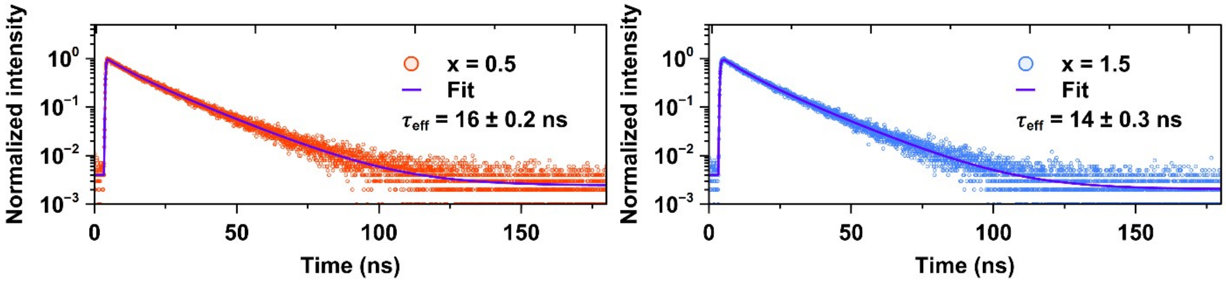

Figure S4. RT photoluminescence decay times of Pr^{3+} ions (λ_{exc} = 280 nm, λ_{emi} = 320 nm) in the Pr^{3+}-doped $Lu_{1.5}Y_{1.5}Al_{5-x}Sc_xO_{12}$ crystals, where x = 0.5 and 1.5.

Figure S4 shows representative decay curves of Pr^{3+} emission recorded at 320 nm, following excitation at 280 nm, for the Pr^{3+}-doped $Lu_{1.5}Y_{1.5}Al_{5-x}Sc_xO_{12}$ crystals, where x = 0.5 and x = 1.5. The emission at 320 nm corresponds to the interconfigurational $4f^15d_1^1 \rightarrow 4f^2$ transition, which occurs on a nanosecond timescale. The decay curves exhibit multi-exponential behavior due to the complex relaxation dynamics of the Pr^{3+} ions in the host crystal. Each curve was fitted using a multi-exponential decay model according to Equation 1. To enable quantitative comparisons of the temperature-dependent evolution of the decay behavior, the mean decay time ($\tau_{effective}$) was computed according to Equation 2. The mean decay time shows a linear acceleration with increasing Sc^{3+} ions concentration.

Table S2. Comparison of maximum band position and full width at half maximum (FWHM) of the interconfigurational $4f^15d_1^1 \rightarrow 4f^2$ emission bands of Pr^{3+} ions across various multicomponent garnet host materials.

Materials	**Maximum band position (nm)**	**FWHM (nm)**	**Method**	**Year**	**Ref.**
$Lu_3Al_5O_{12}$:Pr	310	89	μ-Pulling down	2024	5
$Y_3Al_5O_{12}$:Pr	320	90	μ-Pulling down	2013	6
$Lu_{2.25}Y_{0.75}Al_5O_{12}$:Pr	318	93	Czochralski	2019	7
$Lu_2Y_1Al_3Ga_2O_{12}$:Pr	315	101	μ-Pulling down	2012	8
$Gd_3Al_3Ga_2O_{12}$:Pr	330	30	μ-Pulling down	2012	9
$Y_3Al_3Ga_2O_{12}$:Pr	313	100	μ-Pulling down	2013	10
$Gd_2Y_1Al_3Ga_2O_{12}$:Pr	315	25	μ-Pulling down	2013	10
$Lu_{1.5}Y_{1.5}Al_5O_{12}$:Pr	312	90	μ-Pulling down	This work	
$Lu_{1.5}Y_{1.5}Al_{4.5}Sc_{0.5}O_{12}$:Pr	311	91	μ-Pulling down		
$Lu_{1.5}Y_{1.5}Al_4Sc_{1.0}O_{12}$:Pr	310	92	μ-Pulling down		
$Lu_{1.5}Y_{1.5}Al_{3.5}Sc_{1.5}O_{12}$:Pr	306	92	μ-Pulling down		
$Lu_{1.5}Y_{1.5}Al_3Sc_{2.0}O_{12}$:Pr	305	103	μ-Pulling down		

Table S2 provides a detailed overview of the spectroscopic parameters, including the peak band position and full width at half maximum (FWHM), associated with the interconfigurational $4f^15d_1^1 \rightarrow 4f^2$ emission transitions of Pr^{3+} ions across various multicomponent garnet host matrices. The results reveal that Sc substitution significantly intensifies structural disorder within the host lattice. This observation holds important potential for the design of disordered host lattices, particularly in the advancement of high-performance optical materials. By exploting the increased structural disorder, it becomes possible to optimize absorption coefficients and broaden emission bands, key factors for enhancing the functionality of laser materials and phosphors.

4. Luminescence Properties Under Synchrotron Radiation

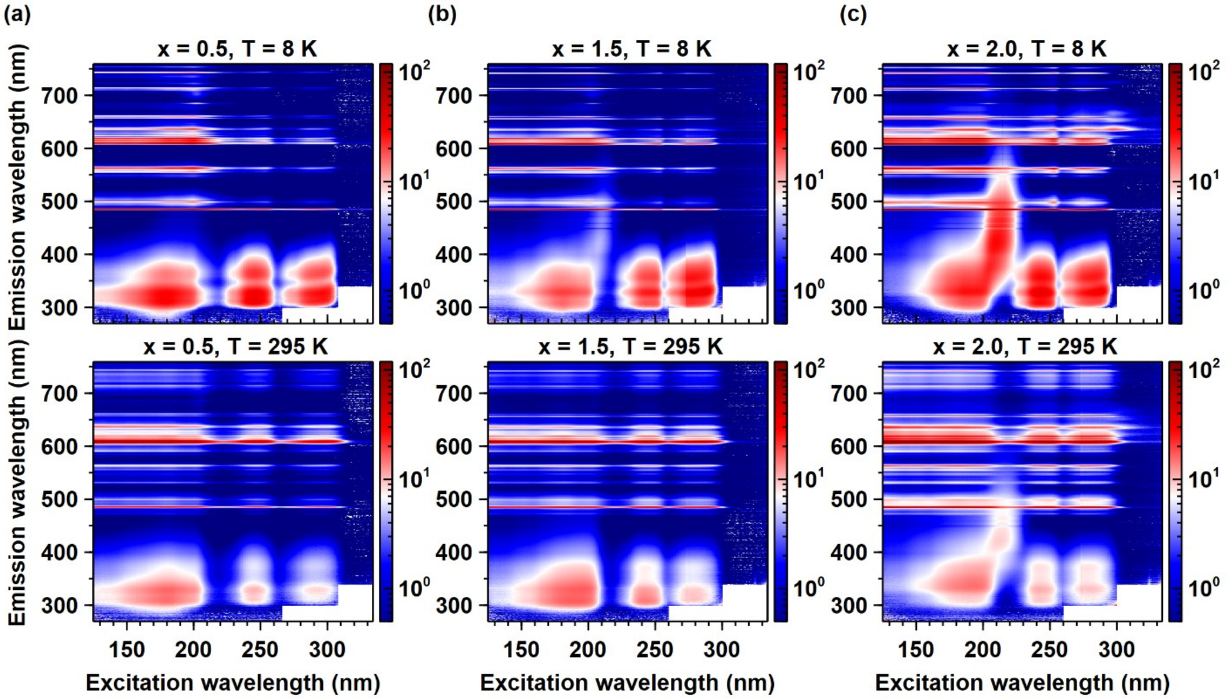

Figure S5. 2D excitation-emission maps (EEM) presented for temperatures of 8 K (upper panels) and 295 K (lower panels) for the Pr^{3+}-doped $Lu_{1.5}Y_{1.5}Al_{5-x}Sc_xO_{12}$ crystal, where (a) x = 0.5, (b) x = 1.5 and (c) x = 2.0.

Figure S5a, S5b, and S5c present a comparative analysis of the excitation-emission maps (EEMs) recorded using synchrotron radiation at temperatures of 8 K (upper panels) and 295 K (lower panels) for the Pr^{3+}-doped $Lu_{1.5}Y_{1.5}Al_{5-x}Sc_xO_{12}$ crystals, where x = 0.5, 1.5 and 2.0. The EEMs indicate that the both interconfigurational ($4f^1 5d_1^1 \rightarrow 4f^2$) and intraconfigurational ($4f^2 \rightarrow 4f^2$) emissions are effectively excited by intraband transitions (with energies exceeding 188 nm) as well as by the interconfigurational excitations ($4f^2 \rightarrow 5d_1^1 4f^1$) with energies below 220 nm. Notably, the EEMs reveal that the interconfigurational $4f^1 5d_1^1 \rightarrow 4f^2$ emission bands broaden and decrease in intensity with increasing Sc^{3+} ions concentration, while the intensity of the intraconfigurational

4f^2 → *4f*^{2} emission shows a corresponding increase. A significant observation is the emergence of a broadband emission ranging between 400 and 520 nm in the Pr^{3+}-doped $Lu_{1.5}Y_{1.5}Al_{5-x}Sc_xO_{12}$ crystals, where x = 2.0. This broadband emission is observed at 8 and 295 K. The disordered and eutectic structure of the Pr^{3+}-doped $Lu_{1.5}Y_{1.5}Al_3Sc_2O_{12}$ (x = 2.0) crystal, combined with the enhanced emission intensity ranging between 400 and 520 nm observed at 8 K, suggests that the origin of this emission intensity may be related to the presence of F^+ and F centers [11, 12].

5. *Temperature dependence of radioluminescence, scintillation and thermoluminescence*

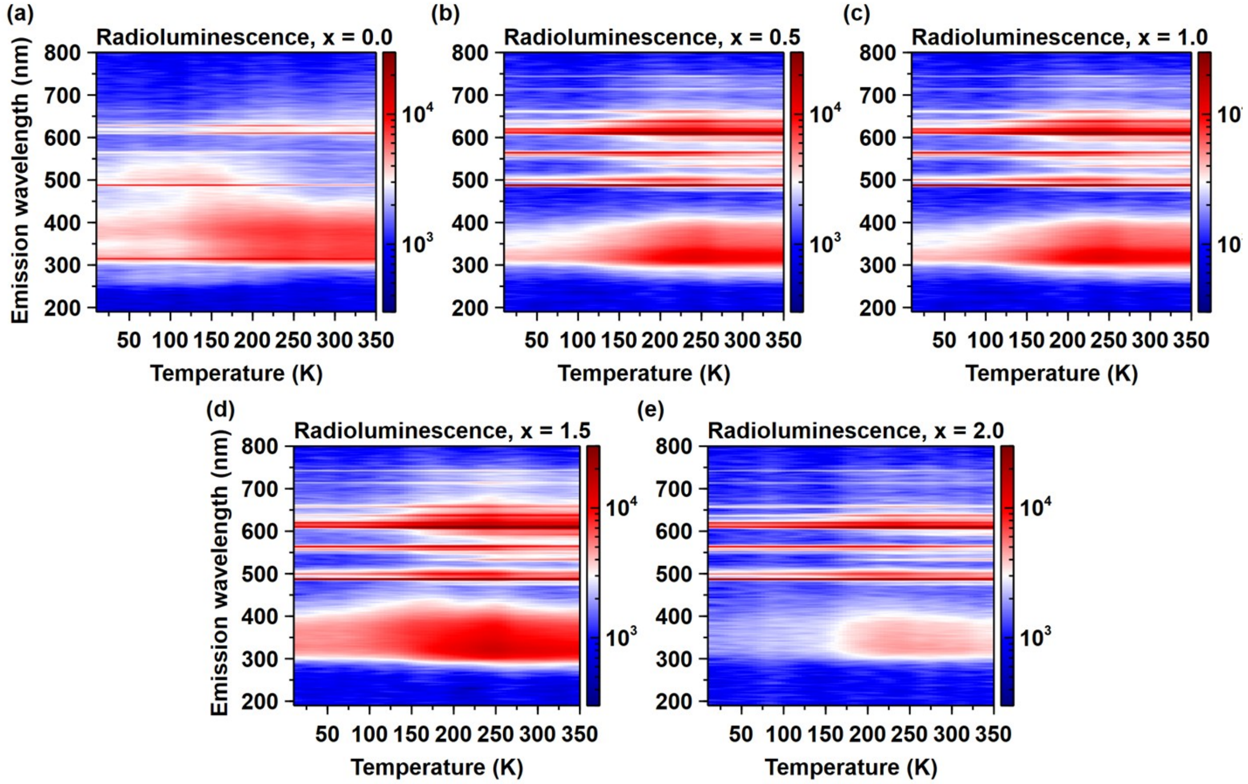

Figure S6. 2D temperature-dependent (10 - 350 K) maps of radioluminescece spectra for the Pr^{3+}-doped $Lu_{1.5}Y_{1.5}Al_{5-x}Sc_xO_{12}$ crystals, where (a) x = 0.0, (b) x = 0.5, (c) x = 1.0, (d) x = 1.5, (e) x = 2.0.

Temperature-dependent (10 - 350 K) two-dimensional radioluminescence spectra of Pr^{3+}-doped $Lu_{1.5}Y_{1.5}Al_{5-x}Sc_xO_{12}$ crystals with varying Sc^{3+} ions concentrations are presented in Figure S6a-e. The radioluminescence maps demonstrate strong correlation with both absorption spectra (Figure

S1) and photoluminescence spectra (Figure 5, 6, S1, S2, and S5). This consistency provides further evidence that Sc admixing significantly disorder the host lattice structure. The results suggest that the progressive lattice distortions introduced by Sc^{3+} ions arise from their larger ionic radius compared to Al^{3+} ions. The incorporation of Sc^{3+} induces strain in the host lattice and alters the local crystal field symmetry surrounding the Pr^{3+} ions. Consequently, an increase in the intraconfigurational $4f^2 \rightarrow 4f^2$ emission intensity is observed with rising temperature and Sc^{3+} ions concentration. Additionally, the enhanced the interconfigurational $4f^1 5d_1^1 \rightarrow 4f^2$ emission intensity observed in Sc-admixed crystals indicates efficient energy transfer pathways from Sc^{3+}-bound excitons to Pr^{3+} luminescent centers.

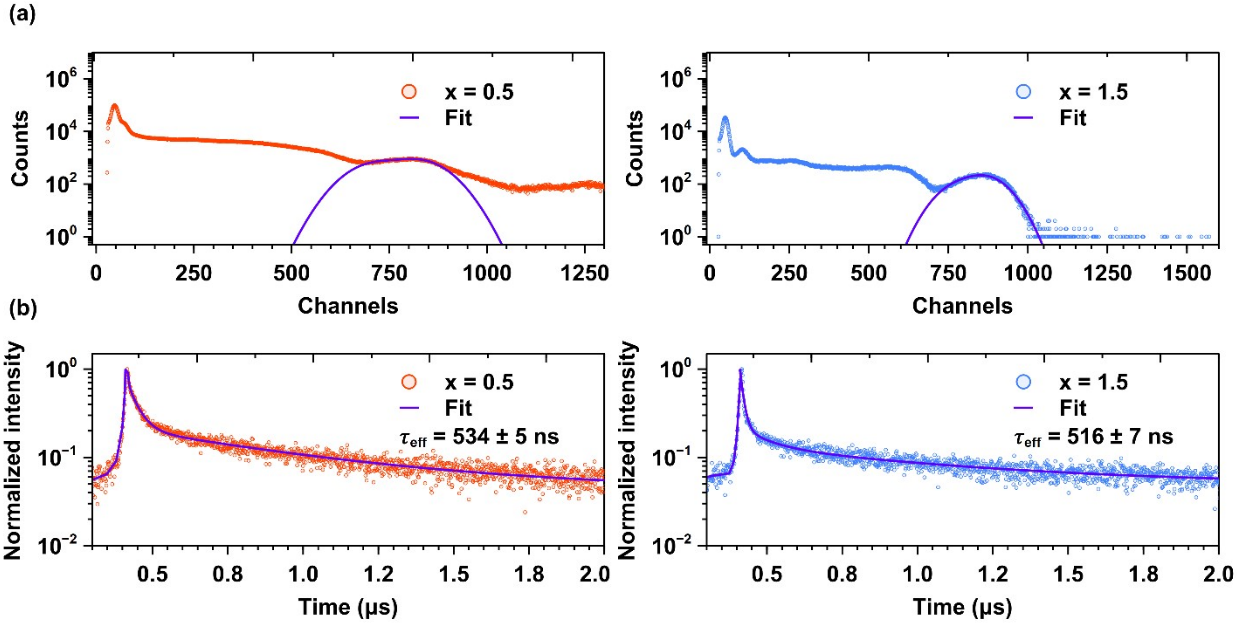

Figure S7. (a) Scintillation light yield values, and (b) decay kinetics under excitation with γ-rays from the ^{137}Cs radionuclide (662 keV) for the Pr^{3+}-doped $Lu_{1.5}Y_{1.5}Al_{5-x}Sc_xO_{12}$ crystals, where x = 0.5 and 1.5.

Figure S7a presents the scintillation light yield values for the Pr^{3+}-doped $Lu_{1.5}Y_{1.5}Al_{5-x}Sc_xO_{12}$ crystals, where x = 0.5 and 1.5, measured under excitation by a ^{137}Cs radioisotope and an amplifier shaping time of 2 μs. The data indicate a significant enhancement in the light yield with increasing Sc^{3+} ions concentration, consistent with the reduced density of deep trapping centers and improved energy transfer efficiency discussed previously in the main text. Figure S7b presents the scintillation decay time profiles for the same crystals under excitation by the ^{137}Cs radioisotope. The results reveal similarities in decay dynamics between the Pr^{3+}-doped $Lu_{1.5}Y_{1.5}Al_{5-x}Sc_xO_{12}$ crystals with x = 0.5 and x = 1.5 showing similar decay time values, which suggests that Sc admixing alters the recombination pathways and the energy migration processes within the host lattice. These observations collectively emphasize the dual impact of Sc admixing: (i) a substantial improvement in light yield, linked to both reduced non-radiative losses and enhanced energy transfer to Pr^{3+} activator ions, and (ii) modified decay characteristics, which reflect changes in the local crystal field environment and trapping mechanisms. These measurements provide insights into how Sc admixing affects scintillation performance, highlighting differences in light yield and decay dynamics for varying Sc^{3+} ions concentrations.

6. Electron paramagnetic resonance

Additional signals are observed in the EPR spectra of the Sc admixed crystals. These signals are likely present in the Pr^{3+}-doped $Lu_{1.5}Y_{1.5}Al_{5-x}Sc_xO_{12}$ crystal, where x = 0.0 as well. However, their identification is impeded by significant overlap with the strong Mn^{2+} signals. As illustrated in Figure S8a, analysis of the Sc admixing level dependencies indicates the presence of five distinct signals (labeled S_1-S_5). Notably, the S_4 signal vanishes for the Pr^{3+}-doped $Lu_{1.5}Y_{1.5}Al_4Sc_1O_{12}$ (x = 1.0) crystal, whereas the S_5 signal remains observable even for the Pr^{3+}-doped $Lu_{1.5}Y_{1.5}Al_3Sc_2O_{12}$ (x = 2.0) crystal. Figure S8b displays the double integral intensities of signals S_1-S_3, which differ markedly from one another. Furthermore, only the S_4 and S_5 signals exhibit a multicomponent structure. This feature is not attributable to the zero-field splitting that typically gives rise to fine structure in spin systems with $S > 1/2$ [13], rather, it results from the electron spin ($S = 1/2$) and its hyperfine coupling with adjacent nuclei [14].

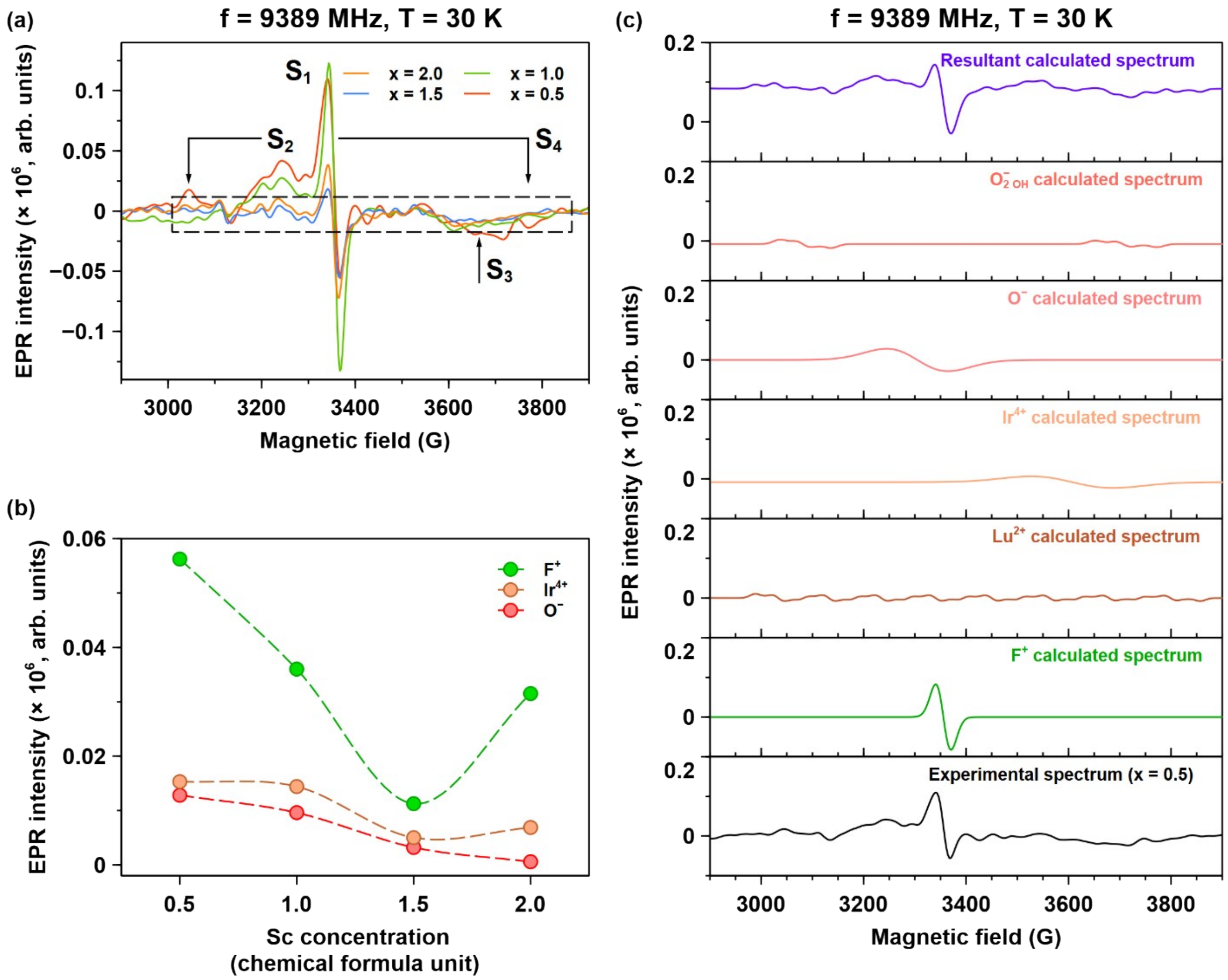

Figure S8. (a) Charge trapping signals S_1-S_5 measured in the Pr^{3+}-doped $Lu_{1.5}Y_{1.5}Al_{5-x}Sc_xO_{12}$ crystals with increasing Sc^{3+} ions concentration. (b) Dependence of the double integral intensities of signals S_1-S_3 on the Sc admixture concentration. (c). The experimental spectrum (Exp.) of the Pr^{3+}-doped $Lu_{1.5}Y_{1.5}Al_{5-x}Sc_xO_{12}$ (x = 0.5) crystal presented alongside the calculated spectra (Calc. - indicates a calculated paramagnetic center). The calculated spectra illustrate the components originating from O^- defect, F^+ center, Lu^{2+}, Ir^{4+} and hydrogen-related $O_2^-{}_{OH}$ centers.

The S_4 signal appears as a doublet with a substantial spectral splitting of approximately 700 G. This observation implies that the nucleus responsible for this hyperfine splitting must exhibit a high Larmor frequency, making hydrogen the most plausible candidate. Similar splitting observed in SiO_2, which has been attributed to hydrogen [15] further supports this interpretation. Additionally, the potential adsorption of OH$^-$ groups from ambient air onto the $Lu_{1.5}Y_{1.5}Al_{5-x}Sc_xO_{12}$ crystal surface cannot be excluded. Consequently, electron capture at a structural oxygen site in the $Lu_{1.5}Y_{1.5}Al_{5-x}Sc_xO_{12}$ adjacent to an OH$^-$ group may lead to the formation of an $O_2^-{}_{OH}$ center.

The S_5 signal exhibits approximately eight distinct components, which can be attributed to hyperfine splitting induced by ^{71}Lu nuclei (I = 7/2, 100% natural abundance). Given that the splitting between adjacent components can reach up to 50 G, it is plausible to associate this feature with the formation of Lu^{2+} centers, characterized by a 5d^1 outer electron configuration (S = 1/2).

The S_1-S_3 signals appear as single-component features, indicating that the electron spin in each case is S = 1/2. The S_1 signal exhibits a *g* factor of 1.999, a value typical for systems with less than half-filled outer shells and consistent with those observed for F$^+$ centers (an electron trapped at an oxygen vacancy, V_O^{2+}: $V_O^{2+} + e^- \rightarrow V_O^+$ (F$^+$) [16]. Accordingly, the origin of the S_1 signal is attributed to an F$^+$ center.

In contrast, the S_2 signal is considerably broad and appears at a *g* factor of approximately 2.03. This value is characteristic of systems with more than half-filled outer shells and falls within the range of *g* factors typical for O$^-$ centers (i.e., a hole trapped at an oxygen anion) [17]. Thus, the S_2 signal is most likely associated with an O$^-$ centre. Similarly, the S_3 signal is broad and observed at a *g* factor of about 1.9, a range that is typical for transition metal ions. Given that the samples were grown using an iridium crucible and considering that iridium can be incorporated into the crystal structure during growth, it is plausible to attribute the S_3 signal to Ir^{4+} centers. With an outer electron configuration of $5d^5$, these centers are expected to adopt a low-spin state (S = 1/2) [18]. To validate these assignments for the S_1-S_5 signals, the experimental EPR spectrum measured in the Pr^{3+}-doped $Lu_{1.5}Y_{1.5}Al_{4.5}Sc_{0.5}O_{12}$ (x = 0.5) crystal was approximated by a calculated spectrum that considered contributions from all five signals (S_1-S_5). The following spin-Hamiltonian was used:

$$\hat{H} = \beta \hat{S}\hat{g}B + A\hat{S}\hat{I}, \tag{6}$$

where $\hat{g}$, $\hat{S}$, $\hat{I}$, are the *g* tensor, electron and nuclear spin operators, respectively. Figure S8c presents the experimental EPR spectrum alongside the calculated spectra for each of the individual S_1–S_5 signals.

The theoretical spectrum demonstrates strong correlation with the experimental data, exhibiting notable consistency across the measured range. Minor discrepancies between the calculated and experimental spectra can be attributed to the complex nature of the spectral composition, which comprises a minimum of five distinct contributions. The complexity of the analysis necessitates the simultaneous optimization of multiple spectral parameters, making the fitting procedure particularly challenging. The derived parameters, comprehensively presented in Table 2, fall within the expected ranges for their respective spectral components (S_1-S_5). The positioning of these values within established literature ranges validates the computational approach and confirms the accurate determination of the spectral parameters. The agreement between theoretical predictions and experimental observations substantiates the reliability of the fit assignment and the overall spectral interpretation.

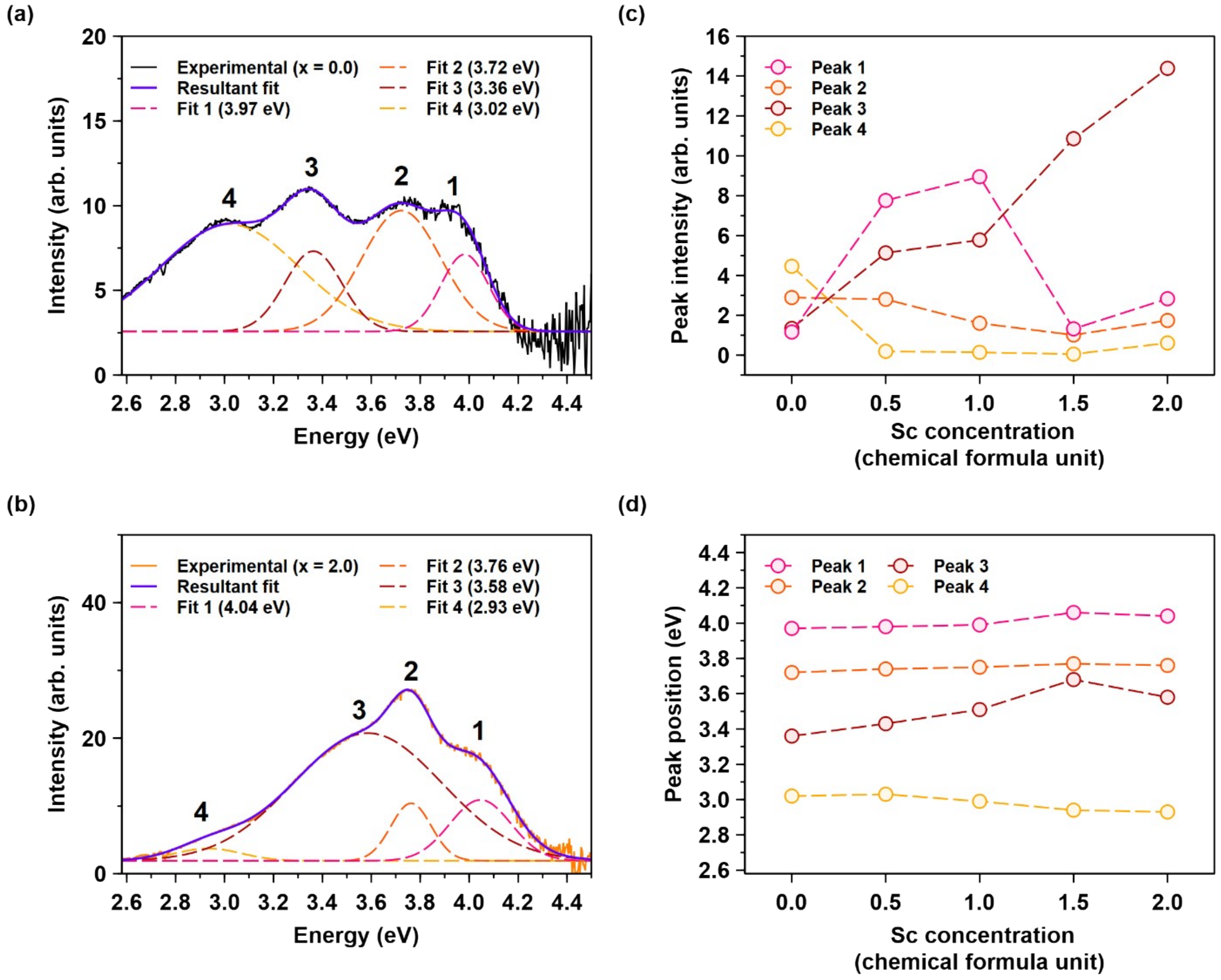

Figure S9. Emission spectra of the Pr^{3+}-doped $Lu_{1.5}Y_{1.5}Al_{5-x}Sc_xO_{12}$ crystals for (a) x = 0.0 and (b) x = 2.0 at 8K, excited at 6.52 eV. The spectra are deconvoluted into four individual Gaussian fits. (c) Dependence of fit intensities (arbitrary units) for Fits 1–4 on Sc concentration. (d) Evolution of fit positions (eV) as a function of Sc^{3+} ions concentration.

The presented emission spectra of the Pr^{3+}-doped $Lu_{1.5}Y_{1.5}Al_{5-x}Sc_xO_{12}$ crystals, where x = 0.0 and 2.0 at 8K under 6.52 eV excitation reveal significant variations in fit positions and intensities as a function of scandium substitution. The Gaussian deconvolution of the spectra identifies four distinct optical transitions. Fits 1 and 2, corresponding to the interconfigurational $4f^15d_1^1 \rightarrow 4f^2$ transitions of Pr^{3+} ions, exhibit a blue shift with Sc^{3+} ions concentration. This spectral shift suggests a modification in the local crystal field, likely caused by the difference in ionic radii between Sc^{3+} (r_{VI} = 0.745 Å) and Al^{3+} (r_{VI} = 0.535 Å), altering the Pr^{3+} coordination environment. Furthermore, Fit 3, attributed to the superposition of Pr^{3+} and F^+ luminescence, undergoes a notable blue shift from 3.36 eV to 3.58 eV, suggesting an increased interaction between Pr^{3+} and intrinsic defect states. The enhancement in Fit 3 intensity further supports this hypothesis, implying a greater contribution from defect-assisted recombination pathways in the Pr^{3+}-doped $Lu_{1.5}Y_{1.5}Al_3Sc_2O_{12}$ (x = 2.0) crystal. Conversely, Fit 4, associated with F^+-O^- defect pairs, exhibits a red shift from 3.02 eV to 2.93 eV, indicating structural distortions. The spectral broadening and intensity variations observed in the Pr^{3+}-doped $Lu_{1.5}Y_{1.5}Al_3Sc_2O_{12}$ (x = 2.0) crystal suggest an increased defect-assisted recombination contribution and the formation of garner-cubic bixbyite-like distorted perovskite hypoeutectic, which influence the material's luminescence efficiency and decay dynamics. The good agreement between the cumulative fit and the experimental data further validates the Gaussian decomposition methodology employed in this study. These findings highlight the role of Scincorporation in tuning the optical properties of Pr^{3+} ions in garnet crystals, providing valuable insights into their potential applications in luminescent and scintillation materials.

The systematic evolution of fit intensities and positions with increasing Sc^{3+} ions concentration, see Figure S9c-d, supports the mechanisms proposed based on the EPR data, see Figure 9, Figure S8, Figure S9a-b as well as related discussion. The evolution of fit intensities, as illustrated in Figure S9c, indicates that increasing Sc^{3+} ions concentration preferentially enhances the intensity of Fit 3 while suppressing the contributions of Fits 1, 2, and 4. This trend suggests that Sc^{3+}

incorporation modifies the electronic structure of the host lattice, thereby altering the relative contribution of Pr^{3+}- and defect-mediated recombination channels. The pronounced enhancement of Fit 3 at higher Sc concentrations implies that Sc substitution stabilizes the mixed Pr^{3+}-F^{+} emission pathway, possibly by reducing charge-carrier trapping at defect sites. In addition to intensity variations, the systematic shift in fit positions with Sc incorporation, as shown in Figure S9d, provides further insight into the structural modifications occurring within the lattice. The blue shift of Fit 3 suggests a modification in the local crystal field surrounding the Pr^{3+} ions, potentially arising from an increase in lattice distortion as Sc^{3+} ions replace Al^{3+}. In contrast, the red shift observed for Fit 4 implies that defect-related emission centers experience an altered electronic environment, possibly due to changes in defect charge compensation mechanisms. The observed trends highlight the significant role of Sc substitution in tailoring the luminescence properties of the Pr^{3+}-doped $Lu_{1.5}Y_{1.5}Al_{5-x}Sc_xO_{12}$ crystals. The enhanced mixed emission pathway (Fit 3) at higher Sc^{3+} ions concentration~~s~~ suggests a potential strategy for optimizing the material's photoluminescence characteristics for optoelectronic applications. Moreover, the suppression of defect-mediated luminescence at higher Sc^{3+} ions concentration indicates that controlled Sc-doping may serve as a means of minimizing non-radiative recombination processes, thereby improving the overall efficiency of Pr^{3+}-based luminescent materials.

Declaration of Competing Interest

The authors declare that they have no known competing financial interests or personal relationships that could have appeared to influence the work reported in this paper.

Acknowledgments

This project has received funding from the European Union's Horizon Europe research and innovation programme under the Marie Skłodowska-Curie Actions COFUND, Physics for Future, grant agreement No 101081515, the National Science Centre Poland (NCN) No.: 2020/39/D/ST3/02711 and the GIMRT program of the Institute for Materials Research, Tohoku University Proposal No. 202306-RDKYA-0533. The financial support of the Leading Agency National Science Centre - Czech Science Foundation project No. 24-14580L is gratefully acknowledged.

References

1. M. Poulos, S. Giaremis, J. Kioseoglou, J. Arvanitidis, D. Christofilos, S. Ves, M. P. Hehlen, N. L. Allan, C. E. Mohn and K. Papagelis, *J Phys Chem Solids*, 2022, **162**.
2. Y. F. Chen, P. K. Lim, S. J. Lim, Y. J. Yang, L. J. Hu, H. P. Chiang and W. S. Tse, *Journal of Raman Spectroscopy*, 2003, **34**, 882-885.
3. A. Markovskyi, P. Radomski, W. Dewo, V. Gorbenko, A. Fedorov, T. Runka and Y. Zorenko, *Mater Res Bull*, 2025, **182**.
4. W. Dewo, V. Gorbenko, Y. Zorenko and T. Runka, *Optical Materials: X*, 2019, **3**.
5. K. Bartosiewicz, B. Albini, D. Szymański, P. Socha, T. Horiai, M. Yoshino, A. Yamaji, S. Kurosawa, R. Kucerkova, P. Galinetto and A. Yoshikawa, *J Alloy Compd*, 2024, **985**.
6. K. Sreebunpeng, W. Chewpraditkul, V. Babin, M. Nikl and K. Nejezchleb, *Radiation Measurements*, 2013, **56**, 94-97.
7. C. Foster, Y. Wu, L. Stand, M. Koschan and C. L. Melcher, *J Lumin*, 2019, **216**, 116751.
8. K. Kamada, T. Yanagida, J. Pejchal, M. Nikl, T. Endo, T. Kousuke, Y. Fujimoto, F. Akihiro and A. Yoshikawa, *IEEE Transactions on Nuclear Science*, 2012, **59**, 2130-2134.
9. K. Kamada, T. Yanagida, J. Pejchal, M. Nikl, T. Endo, K. Tsutumi, Y. Usuki, Y. Fujimoto, A. Fukabori and A. Yoshikawa, *J Cryst Growth*, 2012, **352**, 84-87.
10. M. Nikl, K. Kamada, S. Kurosawa, Y. Yokota, A. Yoshikawa, J. Pejchal and V. Babin, *Phys Status Solidi C*, 2013, **10**, 172-175.
11. K. Bartosiewicz, T. Horiai, A. Yamaji, A. Yoshikawa, S. Kurosawa, M. Yoshino and Y. Zorenko, *Mater Sci Eng B-Adv*, 2020, **261**.
12. K. Bartosiewicz, T. Horiai, A. Yamaji, A. Yoshikawa, S. Kurosawa, K. J. Kim, V. Vistovskyy, A. Voloshinovskii and Y. Zorenko, *J Lumin*, 2021, **235**.
13. C. P. P. a. H. A. Farach, *Handbook of electron spin resonance*, American Institute of Physics, New York, 1994.
14. J. R. B. J. E. Wertz, *Electron Spin Resonance: Elementary Theory and Practical Applications*, Chapman and Hall, New York, 1986.
15. A. M. Monti, M. Buryi, M. Fasoli and M. Martini, *Radiation Measurements*, 2021, **145**.
16. V. Laguta, M. Buryi, P. Arhipov, O. Sidletskiy, O. Laguta, M. G. Brik and M. Nikl, *Physical Review B*, 2020, **101**.
17. V. V. Laguta, M. Buryi, M. Nikl, J. Rosa and S. Zazubovich, *Physical Review B*, 2011, **83**.
18. A. B. Abragam, B., *Electron Paramagnetic Resonance of Transition Ions*, Oxford University Press, London, England, 2012.